

# Tracking radar echoes by multiscale correlation: a nowcasting weather radar application

Simone Tanelli <sup>a</sup>, Luca Facheris, Fabrizio Cuccoli and Dino Giuli

<sup>a</sup> Dipartimento di Ingegneria Elettronica, Università di Firenze,  
Via di Santa Marta 3, 50139 Firenze, ITALY ,  
E-mail: tanelli@achille.die.unifi.it, facheris@ingfi1.ing.unifi.it

## ABSTRACT

An algorithm for storm tracking through weather radar data is presented. It relies on the crosscorrelation principle as in TREC (Tracking Radar Echoes by Correlation) and derived algorithms. The basic idea is to subdivide the radar maps in Cartesian format in a grid of square boxes and to exploit the so called local translation hypothesis. The motion vector is estimated as the space shift such that corresponding boxes at different times exhibit the maximum correlation coefficient.

The discussed technique adopts a multiscale, multiresolution, and partially overlapped box grid which adapts to the radar reflectivity pattern. Multiresolution decomposition is performed through 2D wavelet based filtering. Correlation coefficients are calculated taking into account unreliable data (e.g. due to ground clutter or beam shielding) in order to avoid strong undesired motion estimation biases due to the presence of such stationary features. Data are gathered through a C-band multipolarimetric doppler weather radar.

Results show that the technique overcomes some problems highlighted by researchers in previous related studies. Comparison with radial velocity maps shows good correlation values; although they may vary depending on the specific event and on the orographic complexity of the considered area, estimated motion fields are consistent with the shift of the pattern determined through simple visual inspection.

## 1 WEATHER RADAR RAINFALL NOWCASTING

Since weather radars are characterized by high spatial and temporal resolutions (e.g., few hundred meters range resolution, few degrees azimuth and elevation resolution, and one complete scan per minute), the storm motion evaluation and tracking has become a basic application of radar meteorology. Nowcasting is exploited for very short term forecasting of atmospheric events, but also for better understanding the dynamics of such turbulent and complex processes. It is possible in this way to evaluate the orographic effects (e.g. localization of echo growth and decay areas) and to assess the kind of the atmospheric process relying on the detection of small or large scale turbulent features. Such informations are of great importance for forecasting storm evolution and as input to hydrological models.

An interesting group of applications relying on the crosscorrelation principle is that described in [1] and in references cited therein, namely the so called TREC (Tracking Radar Echoes by Correlation) and derived algorithms. The reader is referred to [2] for the detailed description of the original TREC technique. The basic idea is to subdivide a couple of maps in Cartesian format and separated by a time lag  $\Delta t$  in identical square boxes with side  $L$ , with their centers separated by a fixed distance  $\Delta b$ . The motion vector  $\underline{v}$  is estimated as the space shift between the two boxes (one at  $t$ , the other at  $t+\Delta t$ ) that exhibit the maximum correlation coefficient. Such approach is often used also in video compression applications to remove temporal correlation between two subsequent frames of a sequence of images [3].

The rationale is to exploit the so called local translation hypothesis: in the ideal case, if a box exists in the image at time  $t+\Delta t$  whose pixels are obtained by rigid translation  $\underline{v}$  of pixels belonging to a box of the image at time  $t$ , the motion vector  $\underline{v}$  is the estimated displacement and the correlation index takes the unit value. In real cases, deformation effects are present in general, preventing from reaching the ideal unit value. However, when such deformations are not excessive, the simple translation model can be locally applied.

The matching of each box belonging to the image at time  $t$  is carried out over a search area of the image at time  $t+\Delta t$  centered in the position of the original box and assuming a maximum displacement equal to  $R_{max}=u_{max}*\Delta t$ , where  $u_{max}$  is the maximum admissible storm velocity.

A critical point of TREC is the determination of  $L$ ,  $\Delta b$  and of the Cartesian grid size  $\Delta G$  of radar data. The researchers who worked on this issue suggested some hints for their optimal choice [1][4]. However, they also pointed out that the choice mainly depends on the rainfall pattern, which on turn depends on the type of rainfall event and on orographic effects. Furthermore, some fine scale features (such as those deriving from ground clutter and shielding by obstacles) heavily influence the storm motion estimation. The optimal choice of such parameters is subject to variations within the same map. Due to the nature of the rainfall process, when the dimension of the box  $L$  is too small with respect to the local scale of the phenomenon, high values of the correlation index can be obtained for several translations, giving thus rise to ambiguity in the estimate of the motion vector. On the contrary, when  $L$  is large enough to include rainfall patterns with independent evolution, the local translation hypothesis is not admissible and a sufficiently high correlation coefficient is not obtained.

The problems illustrated above suggested to improve the TREC technique, as illustrated in [1]. Applying the continuity equation to the field of motion vectors determined by TREC yields a smoother motion vector field void of the anomalies generated by TREC and due to the non optimal choice of  $L$ ,  $\Delta b$  and  $\Delta G$ . This technique was called COTREC (Continuity of TREC vectors).

Here a further approach is adopted according to the following consideration. Block matching by crosscorrelation is particularly efficient when the images have a sufficient level of contrast. This usually does not occur in weather radar maps at the original resolution. It can be observed that only two kind of sharp features may occur typically within a weather radar map: features due to unreliable echoes (i.e., ground clutter effects, shielded beams, non-rain precipitation) and borders of areas of homogeneous kind of rainfall (i.e., convective cells, rainfall due to stratiform systems).

Concerning the former, it has to be highlighted that the presence of areas affected by ground clutter or by absence of data due to shielding (like those shown in Fig. 1), produces highly time-stationary and spatially correlated signatures to which TREC-like algorithms are very sensitive [5], hence providing unreliable estimates of motion in that areas.

This issue was faced as follows. Weather radars exploit the parameters associated with returns from weather targets (amplitude, phase, frequency, polarization), mainly for purposes of qualitative and quantitative observation of precipitation (estimation of rainfall rate and classification of precipitation). Primarily, quantitative estimation is based on the backscattered power per unit volume (reflectivity, in weather radar terminology); in the discussed application the motion estimation technique is applied to the horizontal reflectivity fields ( $Z_H$ ). Other two parameters gathered through a C-band, dual polarization, doppler weather radar station located in Montagnana (Firenze, Italy) are used for classification of echoes: differential reflectivity ( $Z_{DR}$ ) and mean doppler velocity ( $v$ ). The classification technique discussed in [6] allows to mitigate the undesired effects due to the presence of unreliable echoes.

The result of this classification is a Thematic Map (TM) of the rainfall event. A TM example is shown in Fig. 4, together with the original radar maps. Radar data were taken by the polarimetric weather radar data installed in Montagnana (Firenze, Italy) during a storm occurred on June 28, 1994. The system parameters are reported in [7]. For the case study reported here and in the following, the range resolution  $\Delta r=125$  m, the azimuth resolution  $\Delta\theta=1^\circ$  (antenna 3 dB beamwidth), and the resolution in elevation is practically the same. The elevation angle  $\varphi=[2.2+2.7^\circ]$ .

Notice the presence of a strong shielding effect due to an obstacle very close to the radar, yielding a relatively wide area of unreliable pixels. Unreliable pixels are also present in other areas of the maps (in particular in the eastern area) since the Montagnana radar is located in a hilly region, causing remarkable problems of shielding and clutter.

Once the unreliable features are identified a multiresolution (i.e., varying  $\Delta G$ ) and multiscale (i.e., varying  $L$ ) technique may be used in order to perform the matching between boxes such that significantly sharp features are always included and sampled at the optimal spatial resolution.

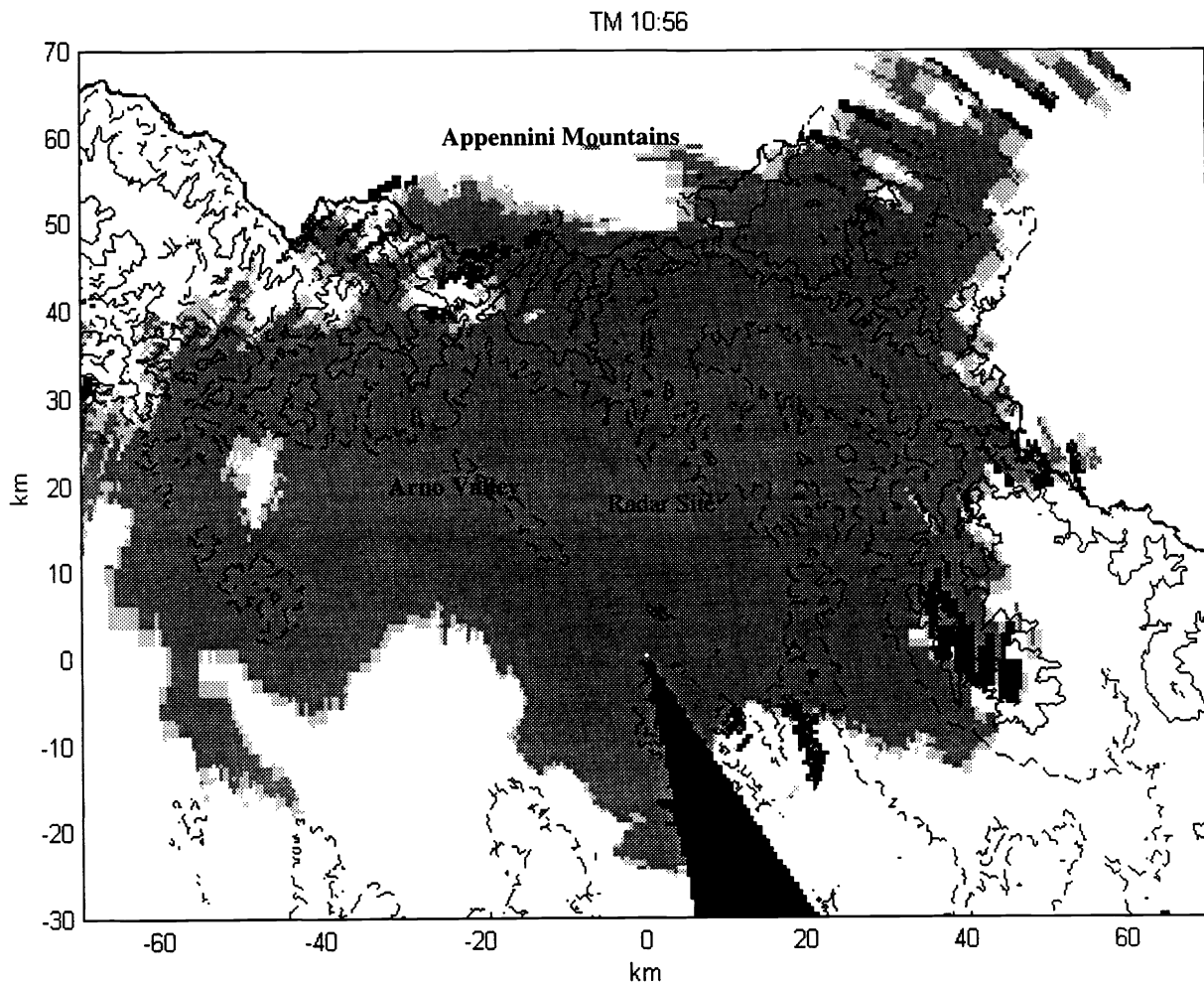


**Fig. (1)** An example of TM: Dark gray='Rain', White='No Echo', Black='Unreliable' (i.e., Totally Shielded or Ground Clutter), Light gray='Edge'. Radar elevation:  $\sim 2^\circ$ . Contour lines at 300 m (dashed) and 800 m (continuous) show the orography of Tuscany. Radar coordinates: (0,0), abscissa orientation: W-E.

In this scenario, the wavelet decomposition gives a very efficient tool for different purposes. Important features of the wavelet analysis are the multiresolution representation of the original data as well as the transformation into a domain where localization both in space and (spatial) frequency is easily performed. Such features are exploited in several 1D and 2D signal processing applications, such as subband coding of images, video and audio signals, transmultiplexers design, echo cancellation in telephone lines, analog scrambling, etc.

## 2 MULTIREOLUTION ANALYSIS OF RAINFALL FIELDS

The theory of the wavelet transform allows to represent a continuous or discrete-time signal at different levels of resolution [8][9][10]. Since its introduction, it raised the interest of the digital signal processing community for its relationship with multirate filter bank theory. Such relationship stimulated new studies and researches in both fields of subband analysis/synthesis bank design and wavelet transform theory, and also developed new possible applications.

A feature related to the wavelet transform is that it yields a multiresolution representation of a signal [10]. In fact, for large values of the scale parameter, the wavelet transform gathers the information contained at low frequencies. The reconstruction obtained from low frequency information represents a smooth version of the signal itself. This information can also be

extracted by the scalar product of the signal  $f(x)$  with a dilated and translated version of a low-pass *scaling* function  $\varphi(x)$ , related to the wavelet function  $\psi(x)$ . Hence, different levels of approximation are defined by

$$Af_{a,b} = \int f(x) \varphi_{a,b}(x) dx \quad (1)$$

where:

$$\varphi_{a,b}(x) = \varphi((x-b)/a) \quad (2)$$

Therefore,  $Af_{a,b}$  is referred to as the *approximation* of  $f$  at a level of resolution defined by the parameter  $a$ . When the parameters  $a$  and  $b$  are sampled as  $a_0^m$  and  $nb_0a_0^m$ , with  $a_0=2$  and  $b_0=1$ , the approximations  $Af_{m,n}$  belong to a subspace of  $L^2(R)$ . These nested subspaces form a multiresolution representation of data, hence allowing the *multiresolution analysis* (MRA). The difference between the approximations  $Af_{m,n}$  and  $Af_{m-1,n}$  is called *detail* signal  $Df_{m,n}$ . It can be shown that the detail signal can be represented through the set of wavelet functions  $\{\psi_{m,n}(x)\}$ . The MRA can be applied to discrete-time signals by considering the sampled data as the highest level of approximation (finest resolution) that is achievable. One of the main results of MRA is that the coefficients of the approximation and detail signal at a given level of resolution can be computed from the upper level approximation coefficients by using low-pass and high-pass digital filters (having  $h(n)$  and  $g(n)$  as impulse responses and  $H(\omega)$  and  $G(\omega)$  as frequency responses, respectively) and downsampling, i.e.,

$$Af_{m,n} = \sum_k Af_{m-1,k} h(2n-k) \quad (3)$$

$$Df_{m,n} = \sum_k Af_{m-1,k} g(2n-k) \quad (4)$$

Such operations are the same as those performed in a filter bank for a two-channel subband decomposition of a digital signal. In an analogous way, the reconstruction of the upper level approximation is performed by using upsampling and filtering, i.e.

$$Af_{m-1,n} = \sum_k Af_{m,k} h'(n-2k) + \sum_k Df_{m,k} g'(n-2k) \quad (5)$$

The scheme is shown in Fig. 1. In the case of orthogonal wavelet decomposition, the synthesis filters are a time-reversed version of the analysis ones and  $G(\omega) = e^{-j\omega} H^*(\omega + \pi)$ , where superscript \* denotes conjugation.

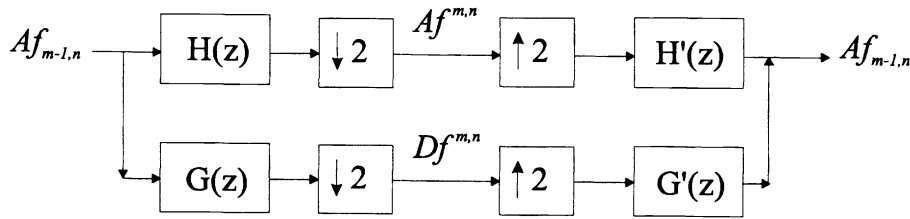


**Fig. (2)** Dyadic wavelet decomposition: approximation and detail coefficients at a given resolution are obtained from the immediately finer resolution level.

The dyadic approach shown in Fig. 2 splits the spectrum of the signal in two frequency subbands. The decomposition may be iteratively applied to the low-pass approximation derived at the previous step. In filter bank theory terminology, this type of filters are said Quadrature Mirror Filters (QMF) or orthogonal filter banks. They allow to achieve the Perfect Reconstruction (PR) of the original signal from its subbands. One disadvantage of QMF banks is that linear phase filters (or equivalently, symmetric wavelets) are excluded from this category, apart from some simple cases, such as the Haar transform.

The decomposition of 2D signals, such as images, is usually obtained by using separable wavelets. This is simply obtained by processing the rows of the image by 1D wavelet analysis and then cascading processing along the columns. As a consequence, the spectrum is divided into four regions: the low-pass region corresponds to the approximation coefficients; the set of three detail signals represents three different high-frequency regions, where horizontal, vertical and diagonal high-frequency components are highlighted. The joint analysis of the four subbands allows to point out possible anisotropy in the image.

Now, spatial localization, anisotropical analysis and MRA are useful when dealing with the analysis of rainfall processes which have been found showing inhomogeneity, anisotropy, and multiscale (i.e., hierarchical structure and clustering) properties [12]. Thus 2D wavelet decomposition proves to be an efficient tool for weather radar map analysis.

In this application of wavelets to weather radar data, Haar wavelet has been used [11]. In fact, Haar filters have the minimum possible length, since

$$h(n) = \frac{1}{\sqrt{2}} \{1, 1\} \quad g(n) = \frac{1}{\sqrt{2}} \{1, -1\} \quad (6)$$

This assures high computational speed as well as the highest spatial localization; the latter property is deemed of highest importance both for ground referencing data and to take into account properly the results of echo classification. Furthermore, the piecewise constant shape of Haar wavelet suitably matches the sharp edges that often characterize rainfall fields (such property is often referred to as intermittency) and to which correlation matching is particularly sensible. Moreover, the approximation coefficients at a given resolution are the values of the measured radar parameters averaged on an area the dimension of which depends on the resolution itself. Hence, the typical techniques of multiparametric classification can be directly applied to them.

### 3 TREMC ALGORITHM

TREMC (Tracking of Radar Echoes by means of Multiscale Correlation). is a storm motion evaluation method based on local crosscorrelation analysis applied to a multiscale decomposition. It differs from TREC in that it operates with not equally sized square boxes and not constant grid size. Each box is thus characterized by its own resolution. A suitable way to implement this strategy is to adopt a hierarchical or multiresolution approach [3]. In this way, it is expected that the aforementioned problems related to the application of TREC can be mitigated, since the choice of the three parameters is adapted to the morphological features of the different zones considered.

The first step of TREMC is resampling the absolute reflectivity maps over a Cartesian grid through bilinear interpolation; for the corresponding TM's, instead, a nearest neighbor method is applied. Then, the sequences of  $Z_H$  maps are decomposed by means of the 2D Haar wavelet. The TREMC method is applied to the approximation coefficients at different resolutions in each map. The classification results obtained using the method described in [6,12] are used in TREMC to eliminate the unreliable pixels from crosscorrelation computations, as well as to roughly estimate the contrast level of the box.

In the following, the generic  $i$ -th box in the map at time  $t$  is denoted with  $B_i^{(t)}$ , with center coordinate vector  $\underline{x}_i^{(t)}$ . The search area over which crosscorrelation at time  $t+\Delta t$  is evaluated is indicated as  $A_i^{(t+\Delta t)}$ . The hierarchical strategy is applied to compute the motion vector (referred to as  $\underline{v}_i^{(t)}$ ) and to define both the box size  $L_i$  and the relative grid size  $\Delta G_i$ . The general scheme of the procedure is the following:

- 1) The "mother box" is defined as the area containing the whole rainfall process within the radar map; its resolution is the coarsest one achieved in the wavelet decomposition.
- 2) The TM relevant to the area covered by the current box is examined to predict whether such box contains sufficient information to obtain a reliable motion vector estimate by means of local matching. Three parameters are calculated and utilized as indicated in Table 1: the number of pixels within  $B_i^{(t)}$  classified as 'Rain' ( $N_{Ri}^{(t)}$ ), 'Unreliable' ( $N_{Ui}^{(t)}$ ) and 'Border' ( $N_{Bi}^{(t)}$ ) are compared with corresponding thresholds ( $N_B$ ,  $N_R$  and  $N_U$ ). When the conditions in the first row of the Table are verified, then local matching based on crosscorrelation is performed, i.e., go to step 3; otherwise, go to step 4, where are described the actions undertaken to change the dimension of the box ('Split' or 'Enlarge'), the grid size ('Refine', i.e., use a finer wavelet approximation coefficients), or to mark the box as not reliably traceable ('Discard').

$N_{Bi}^{(t)} > N_B$	$N_{Ri}^{(t)} > N_R$	$N_{Ui}^{(t)} < N_U$	Action
T	T	T	Local Matching
T	T	F	Split
T	F	T	Refine
T	F	F	Discard
F	T	T	Enlarge
F	T	F	Refine
F	F	T	Discard
F	F	F	Discard

**Table (1)** Decision rules applied in the hierarchical matching algorithm.

$m_i^{(t)} > m_{th}$	$\rho_i^{(t)} < \rho_{th}$	Action
T	T	Refine
T	F	Enlarge
F	--	Split

**Table (2)** Decision rules applied in the hierarchical matching algorithm after local matching is performed.

- 3) *Local Matching*. The crosscorrelation between  $B_i^{(t)}$  and an area in  $A_i^{(t+\Delta t)}$  displaced by a vector  $\underline{v}=(v_x, v_y)$  is computed with  $|\underline{v}| < R_{max}$ . Three parameters are extracted from the matching process: the motion vector  $\underline{v}_i^{(t)}$  maximizing (max. value is 1) the confidence measure, the decorrelation radius  $\rho_i^{(t)}$ , and the confidence measure  $m_i^{(t)}$  calculated here as follows:

$$m_i^{(t)} = 1 - \frac{\min_{(v_x, v_y)} \left\{ \sum_{B_i^{(t)}} (b(k, l) - a(k + v_x, l + v_y))^2 \right\}}{\sum_{B_i^{(t)}} (b(k, l))^2} \quad (7)$$

where  $b(k, l)$  and  $a(k, l)$  are the reflectivity values in the pixel  $(k, l)$  belonging to  $B_i^{(t)}$  or  $A_i^{(t+\Delta t)}$ . Notice that only pixels not classified as 'Unreliable' are used in crosscorrelation computation.

The parameters  $m_i^{(t)}$  and  $\rho_i^{(t)}$  are compared with confidence thresholds  $m_{th}$  and  $\rho_{th}$ , respectively. Table 2 shows the action to be undertaken in step 4 to improve the motion vector field estimate.

- 4) One or more new boxes are generated according to the actions selected at step 2 when no local matching has been performed or after local matching in step 3. The procedures relative to each action are:
- *Refine*. The estimated motion vector  $\underline{v}_i^{(t)}$  is considered reliable and one new box is generated with center coordinates  $\underline{x}_i^{(t)}$  and width  $L_i^{(t)}$ , but with a finer grid resolution equal to  $\Delta G_i^{(t)}/2$ . This corresponds to using a finer wavelet decomposition approximation. If  $\Delta G_i^{(t)}$  is the finest resolution, no refinement occurs.
  - *Enlarge*. This action is undertaken when the crosscorrelation function is too flat around the maximum, due to the lack of sufficient contrast in the box. This may happen, for instance, when the box is completely included in a region of stratiform rain. The vector  $\underline{v}_i^{(t)}$  is not considered reliable, but it is expected that a larger box size will work. Therefore, a new box is generated, having center coordinates  $\underline{x}_i^{(t)}$ , width  $2L_i^{(t)}$  and grid resolution  $\Delta G_i^{(t)}$ . If  $L_i^{(t)}$  is the width of the mother box, no enlargement occurs.
  - *Split*. This action is undertaken when the crosscorrelation function does not reach a sufficiently high value or the box contains too many 'No Echo' points. This may occur when the translation model is still not valid due to other types of movement or deformation. The vector  $\underline{v}_i^{(t)}$  is not considered reliable, but it is expected that the translation hypothesis will be satisfied with a smaller box size. If the finest level of resolution is not achieved, also the level of resolution is changed, so that a sufficient number of pixels is used to compute crosscorrelation. Four new square boxes are obtained by dividing  $B_i^{(t)}$  in four parts, having width  $L_i^{(t)}/2$  and grid resolution  $\Delta G_i^{(t)}/2$ . If  $L_i^{(t)}$  is the minimum box width, no splitting occurs; if  $\Delta G_i^{(t)}$  is the finest resolution, boxes are generated at the same resolution.
  - *Discard*. In this case, it is assumed that no significant features are contained inside the box  $B_i^{(t)}$ ; hence, no further processing is performed on  $B_i^{(t)}$ .
- 5) The process is applied again, starting from step 2, to all the new boxes that have been generated. Let  $B_{i*}^{(t)}$  denote a generic new box generated by  $B_i^{(t)}$ , having center coordinates  $\underline{x}_{i*}^{(t)}$ , box size  $L_{i*}^{(t)}$ , and grid resolution  $\Delta G_{i*}^{(t)}$ , obtained as described in step 4. A new search area  $A_{i*}^{(t+\Delta t)}$  must be defined. The results previously obtained are exploited to position its center  $\hat{\underline{x}}_{i*}^{(t+\Delta t)}$  and the dimension  $\hat{R}_{i*}^{(t+\Delta t)}$  of  $A_{i*}^{(t+\Delta t)}$ . When the new box is generated after local matching,  $\hat{\underline{x}}_{i*}^{(t+\Delta t)}$  and  $\hat{R}_{i*}^{(t+\Delta t)}$  are computed as follows:

$$\hat{\underline{x}}_{i*}^{(t+\Delta t)} = \underline{x}_{i*}^{(t)} + \underline{v}_i^{(t)} \quad (8)$$

$$\hat{R}_{i*}^{(t+\Delta t)} = \rho_i^{(t)} + L_{i*}^{(t)} + \Delta G_{i*}^{(t)} \quad (9)$$

where  $\underline{v}_i^{(t)}$  and  $\rho_i^{(t)}$  are the output of the matching process applied to the box  $B_i^{(t)}$ . When no local matching was performed for the current  $B_i^{(t)}$ ,  $\underline{v}_i^{(t)} = 0$  and  $\rho_i^{(t)} = u_{max} * \Delta t$  were used.

Fig. 3 shows a box  $B_i^{(t)}$  and its best matching area in the search area  $A_i^{(t+\Delta t)}$  displaced by a vector  $\underline{v}_i^{(t)}$ . When the splitting condition applies,  $B_i^{(t)}$  is divided into four boxes. Fig.3 also shows one of these ( $B_{i*}^{(t)}$ ) and the inherited parameters.

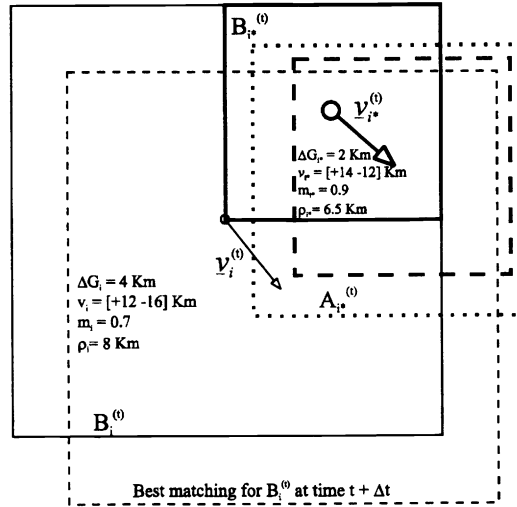


**Fig. (3)** Example of local matching and box splitting.

Once the map has been segmented into several, possibly overlapping, boxes with different resolutions and sizes, the objective is to merge their associated motion vector in a single motion vector field having uniform spacing between vectors. The boxes having a reliable estimate of  $\underline{v}_i^{(t)}$  are used. If the current grid point belongs to a single box, the motion vector is that associated to that box. If it belongs to more than one box, the motion vector is obtained as a weighted average of the associated motion vectors. The weighting coefficient adopted differs slightly from the one proposed in [12] since the calculation of the confidence measure changed, it is a function of the local crosscorrelation, of the decorrelation radius, of the dimension of  $B_i^{(t)}$  and of the spatial resolution associated to the current box. that is:

$$w_i = \frac{\exp(-k(m_i^{(t)})^c)}{\rho_i^{(t)}} \cdot \frac{D_i^{(i)}}{(R_i^{(i)} \cdot L_i^{(t)})} \quad (10)$$

where  $D_i$  is the diameter of the largest circle centered on that grid point and inscribed in  $B_i^{(t)}$ ,  $R_i$  is the spatial resolution and  $k$  and  $c$  are two constants (here 150 and 3 respectively).

#### 4 SIMULATIONS AND RESULTS

TREMC was applied to sequences of radar maps gathered through the multiparameter C-band Polar 55C radar, whose range resolution is 125 m and azimuth resolution is 1 deg. Following the echo classification procedure,  $Z_H$  and  $TM$  maps were resampled on a Cartesian grid with resolution of 500 m. Some disturbing features are the ground clutter areas eastward of the radar station (in particular at 40 km range), and the totally shielded cone in SSE direction due to an obstacle close to the radar. Elevation angle varies between 2 and 3 deg, in order to reduce the effects of other mountainous areas located 40 km NNW and 20 km N from the radar station.

The case study shown refers to an event monitored on June 28, 1994 (data acquisition starting at 10:42 AM - local time- and ending at 11:22). This event has been selected since it produced both convective and widespread patterns; furthermore it developed with easterly wind, hence showing turbulent behaviour due to orographic effects by the Appennini mountains sited north and east with respect to the radar (see Fig. 1).

The main characteristics of the event are visible in Fig. 4. The estimated motion field reveals a fairly constant eastward movement of the core of widespread rainfall. At the same time a general anti-clockwise rotational movement of the precipitating system is evident. Visual inspection of reflectivity patterns shows a general reliability of the algorithm. Since the log scale was adopted for reflectivity, higher emphasis is given to the border areas of the rainfall pattern in the correlation calculations. Therefore, the motion of the very low contrast area in the middle of widespread precipitation was estimated by exploiting only large scale (i.e., 20-80 km wide boxes) estimates: this explains the high continuity of the estimated motion field within that area.

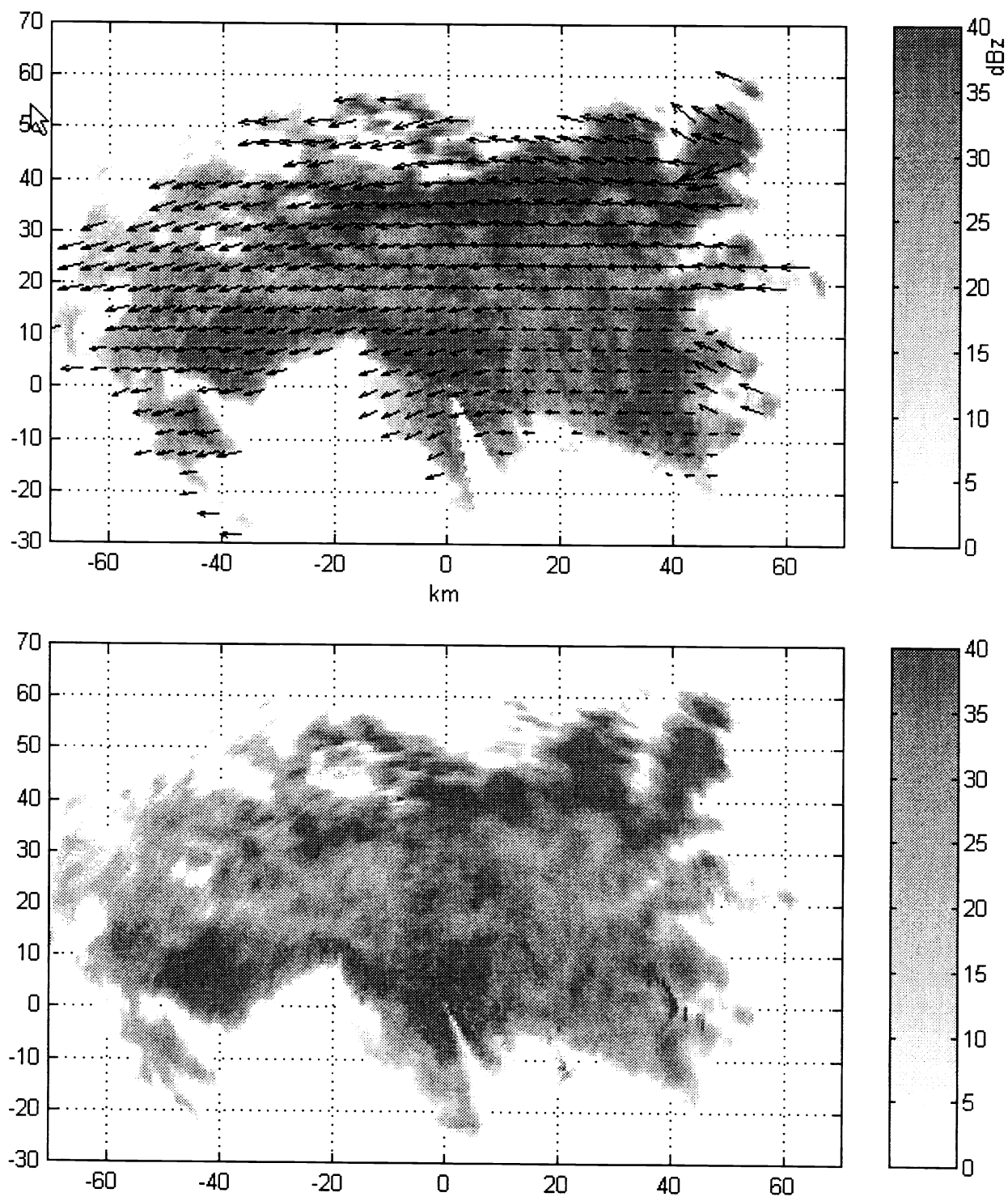


**Fig. (4)** Horizontal reflectivity maps taken at 10:42 and 10:49 AM respectively. Radar site coordinates: (0,0), abscissa orientation: W-E. Estimated motion field is plotted together with the starting map (10:42), arrows show the local unscaled displacement.



TREMC results were also compared with measured mean doppler radial velocities ( $V_d$ ). In this case the radial component of TREMC estimated fields (ME) was calculated on the same polar grid used for doppler measurements. As shown in the scatterplot of Fig. 5, good agreement between TREMC estimates and doppler measurements is obtained over the whole Arno valley area, while poor agreement is found especially in the mountainous area centered 30 km NNE from the radar station and highlighted with a white box in Fig.5. However, from visual appearance of the sequence of reflectivity maps, TREMC estimates seem to be closer to the pattern motion than the doppler measurements. Over the cited area, the module of estimated motion is in good agreement with the module of the radial doppler velocity, while an evident direction error of almost  $90^\circ$  is detected, and attributed to the orographic effect caused by the first slopes of the Appennines. It can be noticed in the scatterplot of Fig. 5 that the rrms (residual root mean square) calculated excluding the white box area is approximately 3 m/s. Since the maps are spaced 7 mins apart, such rrms corresponds to an average error of 1.2 Km approximately, therefore the results of TREMC can be considered satisfactory considering that the finest resolution adopted is 500 m.

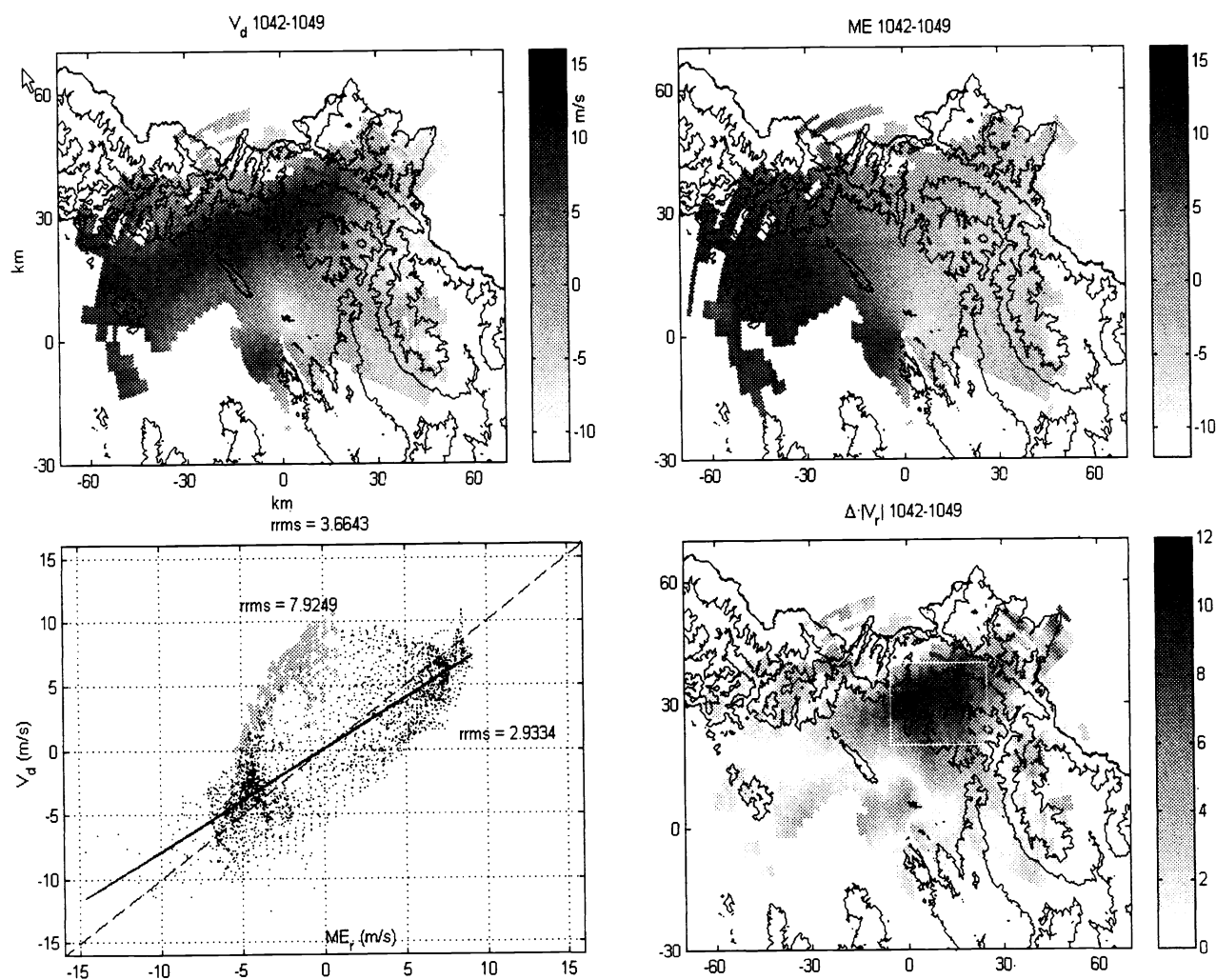


**Fig. (5)** Comparison between motion field estimated through TREMC and doppler mean radial velocities. First three plots in clockwise order represent: mean doppler velocities, estimated motion field and absolute error between the two radial velocity maps. The white box evidences the mountainous area where the largest error occurs. In the scatterplot of ME vs  $V_d$  large grey dots refer to the white box, while small black dots refer to the remaining map. The regression line (continuous) is calculated on the latter.

Cells classified as unreliable (stationary) echoes are not replaced with zero values as in [1]; instead, they are completely removed from the correlation calculations. When such unreliable areas cover a too large portion of the current TREMC box, such box is considered unreliable: only estimates calculated on larger boxes that include the area are considered. The results of this multiscale approach are shown in Fig. 6. See for instance the fairly good motion estimates around the totally shielded cone in SSE direction (TS area in plots) and around the area 40 km eastward affected by severe ground clutter (GC area in plots).

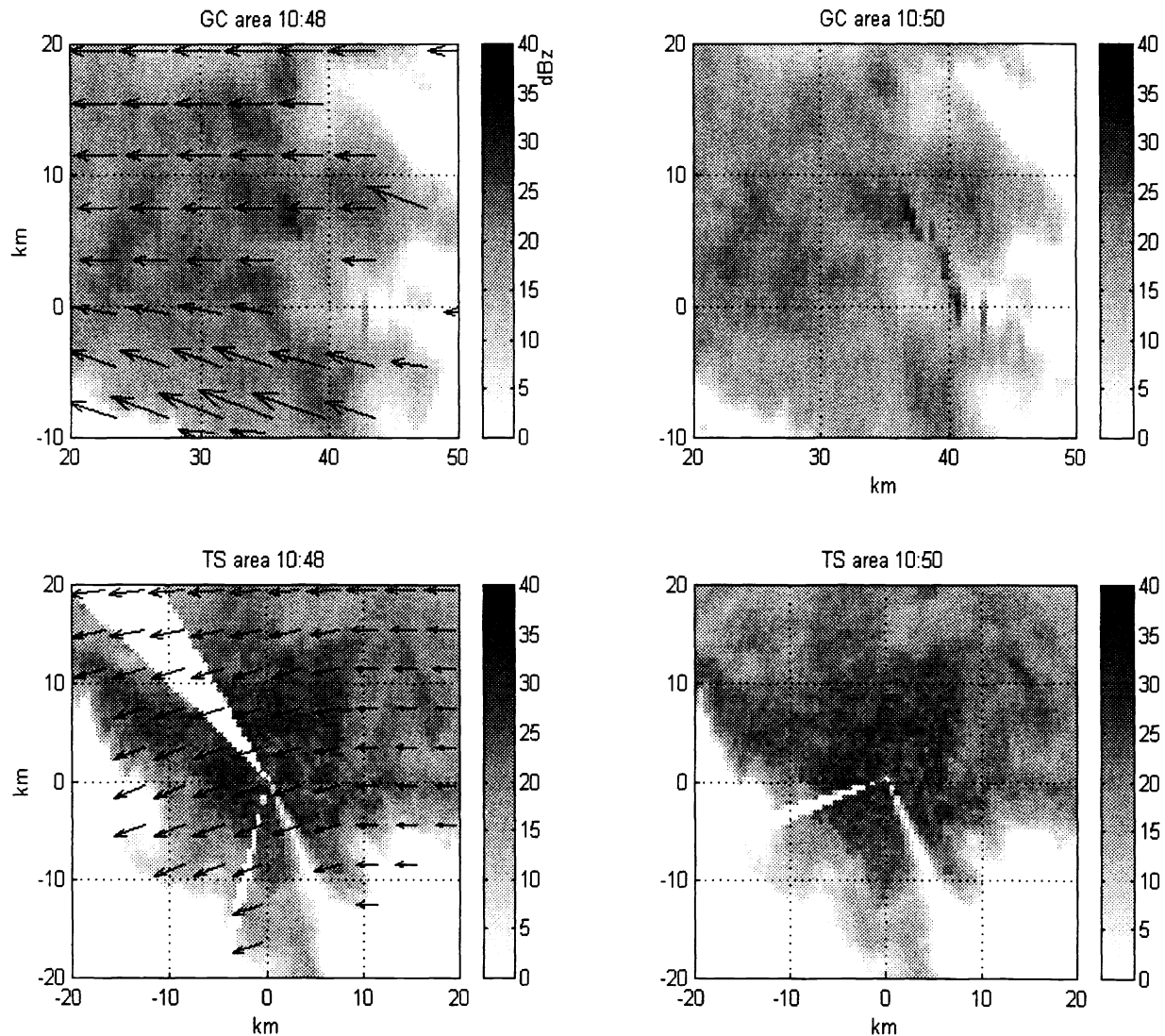


**Fig. (6)** Reflectivity maps relative to two areas including significant undesired stationary features. Coordinates are the same as in Fig. 4. Ground Clutter area includes the mountains at 40 km E from the radar generating the unreliable area shown also in Fig. 1. Total Shielding area includes the main artifact due to an obstacle close to the radar (shown also in Fig. 1), and some data gaps due to missed acquisition. Motion estimated fields calculated on 7 minutes intervals, are shown together with the maps taken at 10:48.

## 5 CONCLUSIONS

In this work, some applications of the wavelet theory to weather radar data processing have been shown. Wavelet are a promising tool for multiresolution analysis applied especially to classification and tracking of such kind of data. In this paper, we focused on the multiresolution aspects, and on the specific problems of the particular application, such as the removal undesired echoes, and tracking of precipitation maps exhibiting simultaneously features at different scales.

An algorithm has been proposed, that reduces the impact of some problems evidenced by the correlation-based algorithms developed by other researchers. The comparison of the algorithm's results with the mean Doppler radial velocities measured by the radar in the same event shows good agreement especially over plane areas: the method could therefore be used over such areas for validating radar Doppler data (in particular providing automatic correction when corrupted by the aliasing phenomenon). In some cases, orography may introduce an apparent disagreement between Doppler maps and the algorithm's predicted velocity. Actually, the most likely hypothesis is that in such cases the Doppler maps refer to low height advection winds, that are the most influenced by orography, while the rainfall pattern motion is mainly affected by advection winds at the cloud level, which are more dependent on large scale atmospheric phenomena.

## 6 ACKNOWLEDGEMENTS

This work was funded by the Italian National Research Council (CNR) through the National Group for the Prevention from Hydrogeological Hazards, and supported by the Italian Ministry for University and Scientific/Technological Research.

## References

1. Li L. Schmid W. and Joss J., Nowcasting of motion and growth of precipitation with radar over a complex orography *Journal of Applied Meteorology*, vol. 34, pp. 1286-1300, 1995.
2. Rinehart R.E. and Garvey E.T., Three-dimensional storm motion detection by conventional weather radar. *Nature*, Vol. 273, pp. 287-289, 1978.
3. Magarey J. and Kingsbury N., Motion estimation using a complex-valued wavelet transform. *Transactions on Signal Processing*, vol. 46, n. 4, 1998, pp. 1069-1084
4. Rinehart R.E., A pattern recognition technique for use with conventional weather radar to determine internal storm motions. Recent process in radar meteorology. *Atmospheric Technology*, pp. 119-134, 1981.
5. Tuttle J.D. and Foote G.B., Determination of boundary layer airflow from a single Doppler radar. *Journal of Atmospheric and Oceanic Technology*. Vol. 7, pp. 218-232, 1990.
6. S.Tanelli, L.Facheris, F. Argenti, D.Giuli: "Wavelet Based Approach for Analysis of Multiparametric Radar Measurements", *Proceedings International Geoscience and Remote Sensing Symposium IEEE*, Seattle (WA), 5-10 luglio 1998, pagg. 449-451
7. Scarchilli G. Gorgucci E. Giuli D. Facheris L. Freni A. and Vezzani G., Arno Project: Radar System and objectives., *Proceedings 25<sup>th</sup> International Conference on Radar Meteorology*, Paris, France, 24-28 June 1991, pp. 805-808
8. Daubechies I., *Ten Lectures on Wavelets*, SIAM Press, Philadelphia, 1992.
9. Vetterli M. Kovacevic J., *Wavelets and subband coding*, Prentice Hall, Englewood Cliffs, NJ 1995
10. Mallat S.G., A theory for multiresolution signal decomposition: the wavelet representation, *IEEE Transactions on Pattern Analysis and Machine Intelligence*. Vol. 11, pp. 674-693, July 1989.
11. Kaiser G., *A Friendly Guide to Wavelets*. Birkhäuser, Boston, 1994
12. L. Facheris, S. Tanelli, D. Giuli, F. Argenti "Wavelet applications to multiparameter weather radar data analysis" to appear on *Information Processing for Remote Sensing*, World Scientific Publishing publication, C.H. Chen Editor